

Spin-Weighted Spherical Harmonics Enable Complete and Scalable $E(3)$ -Equivariant Networks

Chenxing Liang^{1*}, Yuchao Lin^{1*}, Andrii Kryvenko^{1*}, Wendi Yu¹, Chuan Li²,

Jianwen Xie², Xiaofeng Qian^{3,4,5}, Shuiwang Ji^{1,3,6}

¹ Department of Computer Science and Engineering, Texas A&M University

² Lambda, Inc.

³ Department of Materials Science and Engineering, Texas A&M University

⁴ Department of Electrical and Computer Engineering, Texas A&M University

⁵ Department of Physics and Astronomy, Texas A&M University

⁶ Department of Mechanical Engineering, Texas A&M University

Abstract:

$E(3)$ -equivariant networks are promising for 3D atomistic system modeling, yet their scalability is limited by the $O(L^6)$ complexity of the Clebsch-Gordan Tensor Product (CGTP). The recently proposed Gaunt Tensor Product (GTP) reduces the complexity but is unable to capture the antisymmetric paths, resulting in incomplete expressivity. In this work, we present *SpinGTP*, an approach to overcome the GTP incompleteness by generalizing from scalar functions to Spin-Weighted Spherical Harmonics (SWSH). By relying on the algebraic properties of SWSH, SpinGTP recovers the missing antisymmetric interactions while maintaining the asymptotic efficiency of GTP. It also allows for a more expressive equivariant basis that naturally accounts for the parity-odd components of tensor products. We evaluate SpinGTP across diverse benchmarks, including Tetris, 3BPA, SPICE-MACE-OFF, and OC20. Our results show that SpinGTP achieves accuracies comparable to full CGTP. Notably, by explicitly capturing antisymmetric paths, SpinGTP exhibits superior performance in tasks involving chiral materials and non-centrosymmetric geometries. This work provides a complete, scalable, and mathematically rigorous path toward high-order equivariance in large-scale 3D atomistic system simulations.

Keywords: AI for Science, Equivariant Networks, Spin-Weighted Spherical Harmonics, 3D Atomistic Simulations

* These authors contributed equally

 **GitHub Repository:** <https://github.com/divelab/SpinGTP>

Contents

1	Introduction	4
2	Related Work	5
3	Gaunt Tensor Product of Spin-Weighted Spherical Harmonics	5
3.1	Gaunt Tensor Product Efficiency and the Antisymmetry Gap	5
3.2	Spin-weighted Spherical Harmonics for Restoring Expressivity	6
3.3	Real-Basis Spin-Weighted Spherical Harmonics	7
3.4	Parity-Equivariant Spin-Weighted Spherical Harmonics	8
3.5	High-Performance Implementation of SpinGTP	8
3.6	Specialized SWSH Equivariant Layers	9
4	Experiments	9
4.1	Chiral Tetris Classification	10
4.2	3BPA Performance	10
4.3	SPICE-MACE-OFF Chiral Subset Performance	11
4.4	OC20 IS2RE Direct	12
5	Limitations and Summary	13
A	Spin-Weighted Spherical Harmonics (SWSH)	17
A.1	Explicit Formula	17
A.2	Equivariance and Spin-Weighted Transformations	17
A.3	Nonzero Spin-Weighted Gaunt Paths	18
B	Best Asymptotic Runtime Cost	19
C	Real Basis Spin-Weighted Spherical Harmonics	20
C.1	The Unitary \mathbf{Q} Matrix	20
C.2	Example: The \mathbf{Q} Matrix for $\ell = 1$	21
D	Derivation of the Parity-Equivariant Basis	21
E	SpinGTP Implementation and Time Comparison	22

E.1	Tensor Product Implementation	22
E.2	Runtime Comparison	23
F	Training Details	25
F.1	3BPA	25
F.2	SPICE-MACE-OFF Chiral Subset	25
F.2.1	Chirality Classification and Parity Generalization	25
F.2.2	Energy and Force Prediction	27
F.3	OC20 IS2RE	27

1. Introduction

The integration of physical symmetries into deep learning models has become a cornerstone of modern artificial intelligence for physical sciences [36, 5, 32, 16, 7, 8]. By enforcing equivariance, neural networks can model 3D atomic environments with superior data efficiency and generalization compared to standard architectures. Central to these models is the Clebsch-Gordan Tensor Product (CGTP), a fundamental operation that enables interactions between features of different angular frequencies, known as irreducible representations (irreps) [15, 31, 1]. Despite its expressive power, the CGTP suffers from a computational complexity of $O(L^6)$ with the maximum angular degree L . This complexity often forces practitioners to limit L to small values, sacrificing the high-order geometric information necessary for modeling complex molecular interactions and interatomic potentials.

Recent efforts to overcome this bottleneck have focused on accelerating tensor products through alternative mathematical formulations [27, 23]. A notable advance is the Gaunt Tensor Product (GTP) [25], which maps tensor products of irreps to pointwise multiplications of spherical functions in 2D Fourier basis. By leveraging the convolution theorem and Fast Fourier Transforms (FFT), GTP reduces the asymptotic complexity from $O(L^6)$ to $O(L^3)$. However, this efficiency comes with an expressivity loss. GTP retains only coupling paths where the sum of irrep degrees $\ell_1 + \ell_2 + \ell_3$ is even, and removes odd degree-sum paths [34]. These missing paths include antisymmetric interactions such as the $[\ell_1 = 1, \ell_2 = 1, \ell_3 = 1]$ vector cross-product path, as well as couplings needed to form pseudoscalar and axial quantities. This limits scalar GTP on parity-sensitive tasks, especially those involving chiral geometries. We refer to this limitation as the antisymmetric gap.

To address the antisymmetric gap, recent work [35] shows that the antisymmetric paths in scalar GTP can be recovered by lifting scalar spherical signals to irrep-valued signals. Using Vector Spherical Harmonics (VSH), they introduce the Vector Signal Tensor Product (VSTP), which recovers missing antisymmetric paths through generalized Gaunt products with Wigner $9j$ symbol.

In this work, we pursue a more direct mathematical path to this problem by introducing the Spin-Weighted Gaunt Tensor Product (SpinGTP). Rather than lifting scalar spherical signals to vector-valued signals, SpinGTP works directly with Spin-Weighted Spherical Harmonics (SWSHs) and their generalized Gaunt integral with Wigner $3j$ symbols. The spin-weight index replaces the scalar zero-order coupling with a signed spin selection rule, allowing odd degree-sum paths that scalar GTP removes when the required spin sectors are present. We implement this operator in a real, parity-labeled SWSH basis for a rich and concrete representation.

We evaluate SpinGTP on a suite of benchmarks, including the Tetris and large-scale atomistic datasets such as 3BPA [18], SPICE-MACE-OFF [17], and OC20 [6]. Our results demonstrate that SpinGTP-based networks achieves accuracy comparable to full $O(L^6)$ CGTP models while remaining as computationally efficient as the original GTP. Furthermore, we show that our model outperforms previous tensor product methods in predicting properties of chiral materials, showing that the inclusion of antisymmetric paths through SWSH is beneficial for 3D geometric deep learning of chiral geometries.

Our contributions are summarized as follows:

- We propose SpinGTP, an equivariant operation based on SWSH that restores the mathematical completeness to the Gaunt Tensor Product framework.
- We provide mathematical derivations showing that the SpinGTP formulation efficiently recovers the previously missing parity-odd interactions (antisymmetric paths) required for universal E(3) equivariance.
- We evaluate SpinGTP across a range of tasks, including Tetris, 3BPA, SPICE-MACE-OFF, and OC20, demonstrating accuracy comparable to full CGTP while yielding targeted improvements in chiral geometry

modeling through the recovery of antisymmetric paths.

2. Related Work

Equivariant Network Architectures. The landscape of E(3)-equivariant modeling has evolved from early invariant descriptors such as SchNet [29] and DimeNet [9] toward steerable frameworks that leverage irreducible representations (irreps). Seminal architectures like NequIP [4] and Allegro [26] demonstrated the superior sample efficiency of Clebsch-Gordan (CG) tensor products, while the Equiformer series [21, 22] extended these principles to attention-based mechanisms. To alleviate the computational burden of edge-wise products, e2former[20] introduced a node-wise message-passing scheme. While alternative scalarization methods, such as PaiNN [30] and NewtonNet [13] offer increased throughput, they often bypass the full tensor product space, potentially sacrificing the formal universality required for complex geometric.

Tensor Product Acceleration. The Clebsch-Gordan Tensor Product (CGTP) is a standard interaction operator in E(3)-equivariant neural networks [15]. However, direct CGTP scales as $O(L^6)$ with the maximum angular degree L , which limits the use of high-order features. Several recent methods reduce this cost by exploiting structure in equivariant architectures. eSCN [27] aligns features with the edge direction during message passing, which sparsifies the equivariant convolution and reduces it to an SO(2) computation in the local edge frame. [23] reduces tensor-product cost through low-rank tensor decomposition structure. [25] proposed the Gaunt Tensor Product (GTP), which evaluates interactions through spherical harmonic transforms and pointwise products, reducing the complexity to $O(L^3)$. GTP is efficient, but scalar GTP removes odd ℓ -sum paths, including antisymmetric interactions such as the vector cross product [34]. To restore expressivity without reverting to $O(L^6)$ scaling, a Vector Spherical Harmonic (VSH) basis and $9j$ recoupling are introduced to recover missing antisymmetric paths [35]. This framework provides complete algorithm to achieve true asymptotic speedups, reaching $O(L^4 \log^2 L)$ complexity via fast spectral transforms.

3. Gaunt Tensor Product of Spin-Weighted Spherical Harmonics

This section presents the methodology for the Spin-Weighted Gaunt Tensor Product (SpinGTP). We first review the standard Gaunt Tensor Product and identify its main expressivity limitation, the loss of antisymmetric paths with odd ℓ -sum. We then introduce Spin-Weighted Spherical Harmonics (SWSH) and their spin-weighted Gaunt integral. To use this in a real-valued neural network, we build real SWSH bases and extend them with parity labels, allowing the model to represent antisymmetric paths when the required spin channels are present. Finally, we summarize the implementation strategy and the specialized equivariant layers in the architecture.

3.1. Gaunt Tensor Product Efficiency and the Antisymmetry Gap

To reduce the $O(L^6)$ cost of standard Clebsch-Gordan contractions, the scalar Gaunt Tensor Product (GTP) [25] represents equivariant interactions as pointwise products of spherical signals. The resulting coupling is given by a Gaunt coefficient, defined as the integral of two input spherical harmonics against an output spherical harmonic over S^2 such that

$$G_{(\ell_1, m_1)(\ell_2, m_2)}^{(\ell_3, m_3)} = \int_{S^2} Y_{\ell_1 m_1} Y_{\ell_2 m_2} Y_{\ell_3 m_3}^* d\Omega = \sqrt{\frac{(2\ell_1 + 1)(2\ell_2 + 1)}{4\pi(2\ell_3 + 1)}} C_{(\ell_1, m_1)(\ell_2, m_2)}^{(\ell_3, m_3)} C_{(\ell_1, 0)(\ell_2, 0)}^{(\ell_3, 0)}. \quad (1)$$

As shown in Equation (1), GTP retains a subset of Clebsch-Gordan paths where the scalar coupling $C_{(\ell_1, 0)(\ell_2, 0)}^{(\ell_3, 0)}$

is nonzero. This restriction simplifies the interaction, and the spatial product formulation enables an $\mathcal{O}(L^3)$ implementation via fast Fourier transform. The resulting computation can scale to high spectral resolutions that are costly for direct Clebsch-Gordan contractions.

Despite this efficiency, scalar GTP is constrained by the factor $C_{(\ell_1,0)(\ell_2,0)}^{(\ell_3,0)}$, which vanishes whenever $\ell_1 + \ell_2 + \ell_3$ is odd. This removes all odd ℓ -sum coupling paths, including antisymmetric interactions such as the $[\ell_1 = 1, \ell_2 = 1, \ell_3 = 1]$ vector cross-product path. As a result, scalar GTP can fail to distinguish configurations whose signal depends on pseudoscalar or chiral interactions. This limitation motivates the spin-weighted extension introduced below.

3.2. Spin-weighted Spherical Harmonics for Restoring Expressivity

Spin-Weighted Spherical Harmonics (SWSHs) [12] generalize ordinary spherical harmonics by adding an integer spin weight s , alongside the degree ℓ and order m , with $|s| \leq \ell$. The case $s = 0$ recovers ordinary spherical harmonics. For $s \neq 0$, SWSHs represent spin-weighted fields on S^2 and transform by a phase under rotations of the local tangent frame. Additional details are provided in Appendix A.

The role of SWSHs in our tensor product comes from their generalized Gaunt integral. For three SWSHs with the spin weights satisfying $s_3 = s_1 + s_2$, the Gaunt coefficient is

$$\begin{aligned} G_{(\ell_1, m_1, s_1)(\ell_2, m_2, s_2)}^{(\ell_3, m_3, s_3)} &= \int_{S^2} s_1 Y_{\ell_1 m_1} s_2 Y_{\ell_2 m_2} s_3 Y_{\ell_3 m_3}^* d\Omega \\ &= \sqrt{\frac{\prod_{i=1}^3 (2\ell_i + 1)}{4\pi}} \begin{pmatrix} \ell_1 & \ell_2 & \ell_3 \\ m_1 & m_2 & -m_3 \end{pmatrix} \begin{pmatrix} \ell_1 & \ell_2 & \ell_3 \\ s_1 & s_2 & -s_3 \end{pmatrix}. \end{aligned} \quad (2)$$

Unlike the scalar factor in Equation (1), the spin-weighted factor can be nonzero for odd $\ell_1 + \ell_2 + \ell_3$ when proper nonzero spin weights are present. SpinGTP uses this degree of freedom to recover antisymmetric paths that are absent from scalar GTP, while retaining the Gaunt product structure. A more formal statement is presented below and the proof is provided in Appendix A.

Proposition 1: Spin-weighted path completion

Let (ℓ_1, ℓ_2, ℓ_3) satisfy the Clebsch-Gordan triangle rule. Then there exist signed spin weights

$$s_1 \in [-\ell_1, \ell_1], \quad s_2 \in [-\ell_2, \ell_2], \quad s_3 \in [-\ell_3, \ell_3],$$

with $s_3 = s_1 + s_2$, such that the signed-spin path $(\ell_1, s_1) \otimes (\ell_2, s_2) \rightarrow (\ell_3, s_3)$ is not identically zero.

Local Frames and Gauge Dependency. Spin-weighted features depend on a local tangent-frame gauge. Unlike scalar spherical harmonics, an SWSH value ${}_s Y_{\ell m}(\mathbf{x})$ is defined relative to a local orthonormal frame in the tangent plane at \mathbf{x} . If this frame is rotated by an angle ψ , a spin- s field transforms as

$$f_s(\mathbf{x}) \mapsto e^{is\psi} f_s(\mathbf{x}). \quad (3)$$

This gauge dependence means that the basis functions implicitly capture the orientation of the spherical surface, yielding a richer representation than scalar spherical harmonics. However, spin-weighted features can be combined consistently only when their local frame conventions are compatible. In our implementation, frame construction is treated as part of the equivariant architecture. We use explicit geometric frames to evaluate SWSH edge features, with the details described in Appendix A.2.

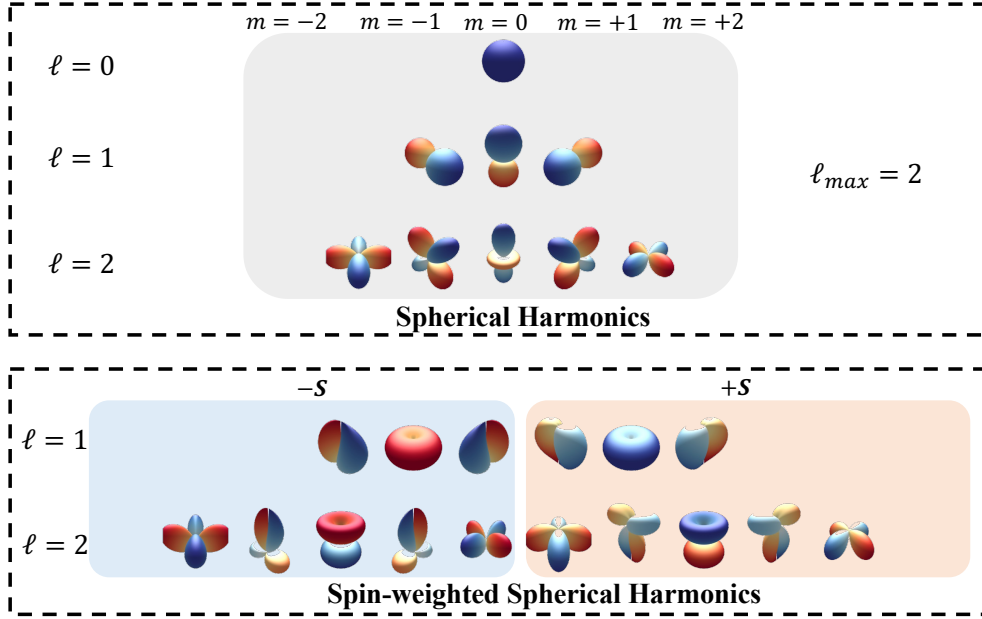


Figure 1: Comparison between standard and spin-weighted spherical harmonics. (a) Scalar spherical harmonics with $\ell_{max} = 2$. The rows represent the basis functions for $\ell = 0, 1$, and 2 , respectively, with the magnetic index m ranging from $-\ell$ to ℓ . (b) Spin-weighted spherical harmonics with $\ell_{max} = 2$ and absolute spin $|s| = 1$. The rows display the basis functions for degrees $\ell = 1$ and $\ell = 2$. For each degree, the basis includes components for both $-s$ and $+s$ across full range of m .

Best Asymptotic Runtime Complexity. For bounded spin weight $|s|_{max} = 1$, SpinGTP can attain the same $O(L^4 \log^2 L)$ asymptotic complexity as the VSTP [35], provided that the FFT-based Gaunt tensor product [25] is used. A proof is given in Appendix B.

3.3. Real-Basis Spin-Weighted Spherical Harmonics

SWSHs are naturally complex-valued, while our network operates on real-valued feature tensors to maintain compatibility with standard activation functions and optimize memory efficiency. For scalar harmonics, the usual real basis can be constructed within a fixed degree ℓ . For spin-weighted harmonics, the construction must also account for the relation

$${}_s Y_{\ell m}^* = (-1)^{m+s} {}_{-s} Y_{\ell, -m}. \quad (4)$$

Following [28], we satisfy Equation (4) by using a **real SWSH basis** that couples the positive and negative spin weights as

$${}_s R_{\ell m} = \begin{cases} \frac{i}{\sqrt{2}} ({}_s Y_{\ell, -m} - (-1)^{-m+s} {}_{-s} Y_{\ell m}) & \text{if } m < 0 \\ {}_s Y_{\ell 0} & \text{if } m = 0 \\ \frac{1}{\sqrt{2}} ({}_s Y_{\ell m} + (-1)^{m+s} {}_{-s} Y_{\ell, -m}) & \text{if } m > 0. \end{cases} \quad (5)$$

For any $|s| > 0$, concatenating both ${}_s Y_{\ell m}$ and ${}_{-s} Y_{\ell m}$ increases the basis dimension from $2\ell + 1$ to $2(2\ell + 1)$ because both signed spin sectors must be retained for real SWSH construction. This doubled representation provides the real spin-weighted features used by the network. A visualized comparison between the real scalar spherical harmonics and the real basis SWSH is provided in Figure 1.

Transformation via the Q Matrix. To connect real feature vectors \mathbf{a}_{real} with the complex Gaunt coefficients used in the tensor product, we use a unitary change of basis \mathbf{Q} such that

$$\mathbf{a}_{\text{complex}} = \mathbf{Q}\mathbf{a}_{\text{real}}.$$

When $|s| = 0$, this is the standard real-to-complex spherical harmonic transformation. For a fixed ℓ and $|s| > 0$, the matrix satisfies $\mathbf{Q} \in \mathbb{C}^{2(2\ell+1) \times 2(2\ell+1)}$ and is organized into four blocks that couple the $\pm s$ and $\pm m$ indices. The explicit block-wise definitions of \mathbf{Q} and the corresponding real-form Gaunt coefficients are given in Appendix C.

3.4. Parity-Equivariant Spin-Weighted Spherical Harmonics

An E(3)-equivariant model must distinguish signals with different parities. Standard scalar spherical harmonics have a fixed parity $P = (-1)^\ell$. For spin-weighted harmonics, spatial inversion also flips the spin weight such that

$${}_s Y_{\ell m}(-\mathbf{x}) = (-1)^\ell {}_{-s} Y_{\ell m}(\mathbf{x}).$$

Thus inversion maps the s sector to the $-s$ sector. As a result, the real basis functions ${}_s R_{\ell m}$ defined in Equation (5) do not by themselves carry a fixed parity when $s \neq 0$. To obtain basis functions with an inversion parity $p \in \{+1, -1\}$, we combine the paired spin sectors and define a **parity-equivariant real SWSH basis**, denoted by $\mathcal{R}_p^{s,\ell,m}(\mathbf{x})$. This construction separates the parity-even and parity-odd components as

$$\mathcal{R}_p^{s,\ell,m}(\mathbf{x}) = \frac{1}{\sqrt{2}} \left({}_{-s} R_{\ell m}(\mathbf{x}) + p(-1)^\ell {}_s R_{\ell m}(\mathbf{x}) \right). \quad (6)$$

By construction, this basis satisfies the required parity constraint $\mathcal{R}_p^{s,\ell,m}(-\mathbf{x}) = p\mathcal{R}_p^{s,\ell,m}(\mathbf{x})$. This allows the representation to distinguish scalar from pseudoscalar channels and polar vector from axial vector channels. A detailed derivation is provided in Appendix D.

The parity-labeled real basis has two roles. First, it lets the network track the inversion parity of each irrep throughout tensor product layers. Second, it provides the necessary geometric signals for physical properties whose sign changes under reflection, including pseudoscalar quantities associated with chiral geometry.

3.5. High-Performance Implementation of SpinGTP

The computational core of SpinGTP is an instruction-based tensor product over SWSH irreps. Each irrep is indexed by $(\ell, |s|, p)$. Given two input feature tensors $\mathbf{x}^{(1)}$ and $\mathbf{x}^{(2)}$, the weighted tensor product maps pairs of input irreps to admissible output irreps as

$$[\mathbf{x}^{(1)} \otimes_{\mathbf{W}} \mathbf{x}^{(2)}]_{\ell_3, s_3, p_3}^{(m_3, w)} = \sum_{u,v} \mathbf{W}_{uvw} \sum_{m_1, m_2} G_{(\ell_1, m_1, s_1), (\ell_2, m_2, s_2)}^{(\ell_3, m_3, s_3)} \mathbf{x}_{u, \ell_1, m_1, p_1}^{(1)} \mathbf{x}_{v, \ell_2, m_2, p_2}^{(2)}, \quad p_3 = p_1 p_2, \quad (7)$$

where G denotes the real SWSH Gaunt contraction and \mathbf{W} mixes feature multiplicities. Internally, the contraction enumerates the signed spin sectors $s = \pm|s|$, applies the selection rule $s_3 = s_1 + s_2$, combines the paired output spin sectors according to the output parity. To balance expressivity with parameter efficiency, we implement *fully connected*, *depthwise*, and *element-wise* tensor products. The implementation details are shown in Appendix E.1.

Pre-contracted Kernel Execution. A direct evaluation of SpinGTP involves many small sparse contractions, which is inefficient on GPUs. Let B denote the number of edges, and let U and V denote the input multiplicities.

When computing over all m_3 , this contraction has time complexity $O(BUV\ell_1\ell_2\ell_3)$. In molecular message passing, the second input $\mathbf{x}^{(2)}$ is often an edge feature with multiplicity $V = 1$. We exploit this structure by precontracting the tensor product kernel with $\mathbf{x}^{(2)}$ before applying it to the node channels.

Based on Equation (7), when the edge multiplicity is one, the sum over v disappears and we first form an edge-dependent kernel

$$\mathbf{K}_{\text{pre}}^{(\ell_3, s_3, p_3)}(m_1, m_3) = \sum_{m_2} G_{(\ell_1, m_1, s_1), (\ell_2, m_2, s_2)}^{(\ell_3, m_3, s_3)} \mathbf{x}_{\ell_2, m_2, p_2}^{(2)}. \quad (8)$$

The remaining contraction becomes

$$[\mathbf{x}^{(1)} \otimes_{\mathbf{W}} \mathbf{x}^{(2)}]_{\ell_3, s_3, p_3}^{(m_3, w)} = \sum_u \mathbf{W}_{u1w} \sum_{m_1} \mathbf{K}_{\text{pre}}^{(\ell_3, s_3, p_3)}(m_1, m_3) \mathbf{x}_{u, \ell_1, m_1, p_1}^{(1)}. \quad (9)$$

This reduces repeated geometric contractions across node channels, and gives a time complexity $O(B\ell_1\ell_2\ell_3 + BU\ell_1\ell_3)$ when computing over all m_3 . In implementation, the precontracted kernel is evaluated as a dense batched matrix multiplication, followed by the learned multiplicity mixing and scatter into the output irreps. The time ablation of this implementation is provided in Appendix E.2.

3.6. Specialized SWSH Equivariant Layers

The SWSH representation requires standard neural network layers to respect the irrep structure indexed by $(\ell, |s|, p)$. We use SWSH linear and normalization layers that mix only compatible feature channels and preserve the type of each irrep.

Equivariant Linear Mixing. The linear layer performs channel mixing within each SWSH irrep. Since features are grouped by $(\ell, |s|, p)$, the linear map is block diagonal across irrep types such that

$$[\text{Linear}(\mathbf{x})]_{\ell, s, p} = \mathbf{W}_{\ell, s, p} \mathbf{x}_{\ell, s, p} + \mathbf{b} \delta_{\ell, 0} \delta_{s, 0} \delta_{p, 1}. \quad (10)$$

Here $\mathbf{W}_{\ell, s, p}$ mixes multiplicities within the same irrep, while the bias is applied only to invariant scalar channels. In practice, identical irrep blocks are grouped in memory so that the blockwise mixing can be evaluated efficiently with batched matrix multiplication.

Equivariant Layer Normalization. Following [21], the normalization layer treats scalar and non-scalar irreps separately. For scalar blocks with $(\ell, s) = (0, 0)$, we subtract the mean over multiplicities before normalization. For all other blocks, no centering is applied. Each block is then normalized by an invariant RMS computed over multiplicities and irrep components. Learnable gains scale each multiplicity channel and are shared across irrep components. Learnable biases are restricted to scalar channels.

4. Experiments

To evaluate the expressivity of the SWSH tensor product, we benchmark our framework across four datasets covering five distinct tasks, ranging from synthetic geometric classification to large-scale atomistic prediction. We first use Chiral Tetris Classification to test whether spin-weighted channels can distinguish enantiomers that scalar Gaunt-based methods cannot separate. We then evaluate energy and force prediction on the 3BPA dataset, which tests generalization across thermally sampled conformations. To assess chiral molecular geometries more directly, we evaluate chirality classification and energy-force prediction on a chiral subset of the SPICE-MACE-OFF dataset. Finally, we integrate the SWSH tensor product into the Equiformer architecture and benchmark it on the Open Catalyst (OC20) IS2RE dataset. Details of datasets, implementations, and comparisons are provided below. Furthermore, to evaluate efficiency, we show the time ablation of our implementations in Appendix E.2.

4.1. Chiral Tetris Classification

Dataset. We first use a minimal synthetic benchmark to test whether the model can represent chiral distinctions. Following [34, 11], the task is to classify eight 3D Tetris-like shapes built from four unit cubes, where the first two classes are non-superimposable mirror images. Each shape is represented as a graph whose nodes are the cube centers, with edges connecting immediately adjacent cubes, and the inputs are presented under random 3D rotations. This makes the benchmark a direct probe of parity-sensitive expressivity rather than a generic shape-classification task.

Training Details. We train an equivariant network with four SpinGTP convolution layers, scalar node inputs, and SWSH edge features on radius-graph edges with cutoff 1.5. The model outputs one odd scalar channel for the mirror pair and six even scalar channels for the other classes, and is trained for 500 Adam steps with fresh random rotations, learning rate 10^{-3} , and MSE loss.

Results. The key question is whether the model can separate the mirror pair. [34] showed that CGTP-based networks solve this task, while scalar GTP fails because it lacks the required antisymmetric interaction. In our experiments, SpinGTP reaches 100% accuracy and correctly distinguishes the two chiral pieces. This shows that the spin-weighted construction provides the missing odd ℓ -sum interaction that scalar GTP cannot express. The Tetris results are shown in Figure 2.

4.2. 3BPA Performance

Dataset. The 3BPA dataset [18] consists of molecular dynamics trajectories of 3-(benzyloxy)pyridin-2-amine, a flexible drug-like molecule with three rotatable bonds that give rise to a complex torsional potential energy surface with many local minima. Following [2, 3, 25], we train on 500 geometries sampled at 300 K. The benchmark evaluates both in-distribution generalization at 300 K and out-of-distribution robustness at 600 K and 1200 K. A dihedral test set further probes the torsional potential energy surface by scanning one dihedral angle while holding the other two fixed, directly testing whether the model correctly resolves conformer transition barriers.

Training Details. We adopt MACE [2] as our base architecture, extended with SWSH-based tensor products, which we refer to as SpinGTP. Training follows a two-stage scheme, with the second stage fine-tuning at an increased relative energy weight. Full details are provided in Appendix F.1.

Results. We compare SpinGTP against Allegro [26], NequIP [4], BOTNet [3], MACE [2], and MACE-Gaunt [25] in Table 1. SpinGTP consistently matches or outperforms current state-of-the-art methods across all test splits. In particular, SpinGTP maintains competitive in-distribution performance at 300 K while

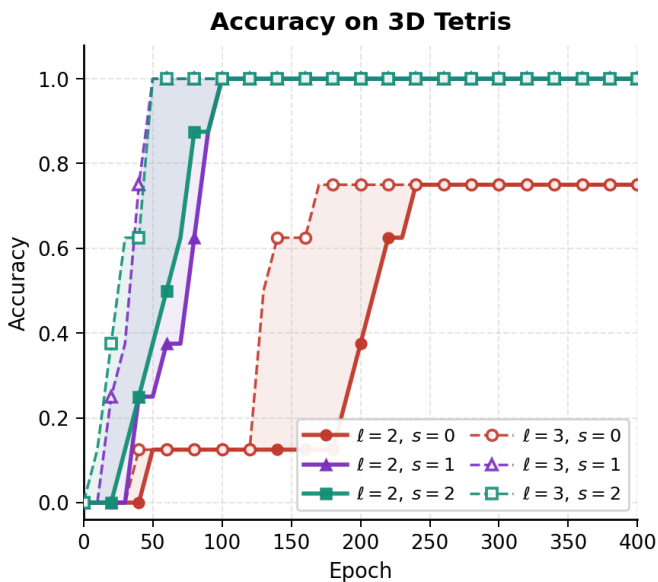


Figure 2: 3D Tetris classification. Scalar GTP ($s = 0$) plateaus at 75%, consistent with its failure to distinguish the chiral mirror pair. In contrast, the SpinGTP with nonzero spin channels reaches 100% accuracy and separates the two enantiomeric pieces, showing that spin-weighted coupling provides the missing odd ℓ -sum interaction.

Table 1: Results on the 3BPA dataset. Root mean square error of Energy (E) in meV and Forces (F) in meV/Å across three temperature regimes and a dihedral scan. Standard deviations over 3 random seeds are in parentheses. **Bold** indicates best performance, underline indicates second best.

		Allegro	NequIP	BOTNet	MACE	MACE-Gaunt	SpinGTP
300 K	E	3.84 (0.08)	3.3 (0.1)	3.1 (0.13)	3.0 (0.2)	2.9 (0.1)	2.9 (0.1)
	F	12.98 (0.17)	10.8 (0.2)	11.0 (0.14)	8.8 (0.3)	9.2 (0.1)	<u>9.0 (0.3)</u>
600 K	E	12.07 (0.45)	11.2 (0.1)	11.5 (0.6)	<u>9.7 (0.5)</u>	10.6 (0.5)	9.6 (0.3)
	F	29.17 (0.22)	26.4 (0.1)	26.7 (0.29)	<u>21.8 (0.6)</u>	22.2 (0.2)	21.0 (0.5)
1200 K	E	42.57 (1.46)	38.5 (1.6)	39.1 (1.1)	<u>29.8 (1.0)</u>	30.4 (1.2)	29.0 (1.1)
	F	82.96 (1.77)	76.2 (1.1)	81.1 (1.5)	<u>62.0 (0.7)</u>	63.1 (1.2)	61.4 (3.2)
Dihedral	E	–	–	16.3 (1.5)	7.8 (0.6)	9.9 (0.3)	8.9 (2.5)
	F	–	–	20.0 (1.2)	16.5 (1.7)	17.7 (1.1)	15.3 (0.7)

showing stronger generalization on the out-of-distribution splits at 600 K, 1200 K, and the dihedral torsion test set. We additionally observe that MACE-Gaunt, despite sharing the same Gaunt-based contraction scheme, underperforms SpinGTP across all splits, with the largest gap on the dihedral torsion test set. This is consistent with our hypothesis that the antisymmetric spin-paths restored by the SWSH tensor product contribute to resolving asymmetric torsional interactions, which are absent in the standard Gaunt contraction used by MACE-Gaunt.

4.3. SPICE-MACE-OFF Chiral Subset Performance

Dataset. The SPICE-MACE-OFF dataset [17] is a large-scale benchmark comprising over 950,000 unique configurations, including small molecules from PubChem, DES370K dimers, and biological systems. To evaluate the specific impact of the SWSH tensor product on chiral expressivity, we curated a chiral subset by screening the original dataset using RDKit [19] to identify enantiomeric pairs and chiral centers via SMILES sequences. This allows us to probe whether the addition of antisymmetric spin-paths translates to improved performance on geometrically sensitive tasks.

Experimental Settings. We evaluate our framework on two distinct categories of tasks. First, we perform chirality classification by modifying the regression heads of [4], MACE [2] and MACE-Gaunt [25] to distinguish between R- and S-chirality. This includes both classification using mixed R/S training data and a parity generalization test, where the model is trained exclusively on R-chirality and evaluated on unseen S-chirality structures. Second, we assess Machine Learning Interatomic Potentials (MLIP) through standard energy and force prediction across four chiral sub-domains: PubChem, Amino Acids, DES370, and Dipeptides.

Chirality Classification and Parity Generalization.

Results for the chirality classification tasks are summarized in Tables 2. In the standard classification task, SpinGTP achieves the fastest convergence, reaching 98% validation accuracy in nearly half the epochs required by MACE-Gaunt (10.9 ± 0.5 vs. 24.3 ± 1.0). The parity generalization test in Table 3 reveals a critical failure mode in the original Gaunt tensor product (MACE-Gaunt), which fails entirely (0% accuracy) to generalize to unseen S-chirality. This stems from the lack of odd-parity paths in standard Gaunt coefficients. In contrast, SpinGTP not only enables this generalization by encoding proper reflection symmetry but also outperforms Clebsch-Gordan (CG) based models, achieving a superior 94.1% accuracy on unseen mirror

Table 2: Chirality classification (R vs. S, both in training). Validation accuracy (%) at selected epochs. Values are reported as mean (std) over 3 runs. Convergence: epochs to first reach 98% validation accuracy (lower is better), also mean (std) over 3 runs.

Model	Epoch 1 \uparrow	Epoch 10 \uparrow	Epoch 20 \uparrow	Best (%) \uparrow	Convergence \downarrow
MACE-Gaunt	64.9 (0.5)	95.5 (0.3)	95.8 (0.3)	98.30 (0.08)	24.3 (1.0)
MACE	67.8 (0.4)	96.8 (0.3)	97.3 (0.2)	98.34 (0.07)	18.2 (0.8)
NequIP	68.1 (0.4)	97.0 (0.2)	97.6 (0.2)	98.43 (0.07)	16.1 (0.6)
SpinGTP	67.4 (0.3)	97.5 (0.2)	98.4 (0.1)	98.79 (0.05)	10.9 (0.5)

structures.

Energy and Force Prediction. Table 4 demonstrates that the completeness of the SWSH tensor product translates to higher accuracy in MLIP tasks. Compared to MACE-Gaunt, our model provides a reduction in both energy and force errors across most of the chiral subsets. Notably, SWSH achieves state-of-the-art performance in the Chiral DES370 and Dipeptides subsets, where sensitivity to complex torsional and chiral interactions is paramount. Even when compared to the computationally heavier Clebsch-Gordan implementations in NequIP and MACE, SpinGTP remains highly competitive, consistently achieving the lowest errors.

Table 3: Chirality parity generalization: train on R-only, evaluate on R-only and S-only. acc_S tests generalization to mirror structures never seen in training. Values are mean (std) over 3 runs.

Model	acc_R (%)	acc_S (%)	Overall (%)
MACE-Gaunt	100.0 (0.0)	0.0 (0.0)	46.3 (0.0)
MACE	100.0 (0.0)	88.6 (1.2)	93.9 (0.7)
NequIP	100.0 (0.0)	90.8 (1.0)	95.0 (0.6)
SpinGTP	100.0 (0.0)	94.1 (0.8)	97.2 (0.4)

Training Setup. Detailed specifications regarding architecture, hyperparameters, and training protocols are provided in Appendix F.2.

Table 4: Results on SPICE-MACE-OFF Chiral Subset. Test set MAE for models trained and evaluated exclusively on SPICE Chiral sub-datasets. Energy (E) in meV/atom, Forces (F) in meV/Å. The best results are shown in **bold** and the second best results are shown with underlines.

Chiral Subset	NequIP		MACE		MACE-Gaunt		SpinGTP	
	E	F	E	F	E	F	E	F
Chiral PubChem	6.1	21.0	<u>5.0</u>	16.0	4.9	19.3	5.7	<u>17.6</u>
Chiral Amino Acids	6.5	20.5	7.5	19.3	<u>6.6</u>	22.9	<u>6.6</u>	<u>19.9</u>
Chiral DES370	3.3	8.4	<u>2.6</u>	<u>6.6</u>	2.9	8.1	2.4	6.3
Chiral Dipeptides	4.0	12.0	4.2	<u>9.7</u>	<u>3.5</u>	11.8	3.2	9.4

4.4. OC20 IS2RE Direct

Dataset. We test whether the SpinGTP implementation remains compatible with large-scale atomistic training. We use the Open Catalyst 2020 (OC20) initial-structure-to-relaxed-energy (IS2RE) task [6], where each system contains an adsorbate on a catalyst slab and the goal is to predict the relaxed energy from the initial structure. These graphs are substantially larger and chemically more diverse than 3BPA and SPICE.

Table 5: Comparison of model performance on energy predictions for OC20 IS2RE-DIRECT validation set without noisy-node auxiliary loss. Our model is trained to compare against several baseline methods, including SchNet [29], DimeNet++ [9], GemNet-dT [10], SphereNet [24], ComENet [33], Equiformer [21] and EquiformerV2 [22]. The best results are shown in **bold** and the second best results are shown with underlines.

MODEL	ENERGY MAE (eV) ↓					EwT (%) ↑				
	ID	OOD Ads	OOD CAT	OOD BOTH	AVERAGE	ID	OOD Ads	OOD CAT	OOD BOTH	AVERAGE
SCHNET	0.6465	0.7074	0.6475	0.6626	0.6660	2.96	2.22	3.03	2.38	2.65
DIMENET++	0.5636	0.7127	0.5612	0.6492	0.6217	4.25	2.48	4.40	2.56	3.42
GEMNET-DT	0.5561	0.7342	0.5659	0.6964	0.6382	4.51	2.24	4.37	2.38	3.38
SPHERENET	0.5632	0.6682	0.5590	0.6190	0.6024	4.56	<u>2.70</u>	4.59	2.70	3.64
EQUIFORMER	<u>0.5088</u>	0.6271	0.5051	0.5545	0.5489	<u>4.88</u>	2.93	4.92	2.98	3.93
EQUIFORMERV2	0.5161	0.7041	0.5245	0.6365	0.5953	-	-	-	-	-
SPINGTP	0.5066	<u>0.6510</u>	<u>0.5130</u>	<u>0.5887</u>	<u>0.5648</u>	5.07	2.58	5.06	<u>2.85</u>	<u>3.89</u>

Following standard OC20 reporting, validation sets are divided into four sub-splits, ID, OOD-Ads, OOD-Cat, and OOD-Both. The direct IS2RE split contains 460k training structures and 100k structures for validation.

Training Details. For the main comparison, we use the direct IS2RE setting without the IS2RS node-level auxiliary task, following the comparison protocol used in Equiformer. Our SpinGTP follows the Equiformer attention backbone and replaces its equivariant tensor-product, linear, and normalization blocks with SWSH counterparts. We use a six-layer SWSH-Equiformer with eight attention heads, cutoff radius 5.0, 128 radial basis functions, on-the-fly periodic graphs, and a maximum of 500 neighbors. Additional architecture and optimization details are provided in Appendix F.3.

Results. Table 5 compares our model against direct IS2RE baselines, including SchNet, DimeNet++, GemNet-dT, SphereNet, Equiformer, and EquiformerV2. Our model achieves performance comparable to Equiformer, which uses Clebsch-Gordan tensor products. In particular, SpinGTP improves the ID split, suggesting that the spin-weighted tensor product retains strong expressive power while remaining compatible with large-scale OC20 training.

5. Limitations and Summary

Limitations. One limitation of SpinGTP is that nonzero spin-weighted features require a consistent gauge. Without compatible frame choices, aggregating spin features can violate equivariance. We address this through geometry-dependent frame construction with a shared convention across nonzero spin irreps (see Appendix A.2), though ambiguity remains for highly symmetric point clouds. Another limitation is that we did not observe a clear acceleration from using the spherical transform, possibly because the multiplicity is large relative to the small L . Resolving these limitations is a direction for future work.

Summary. In this work, we introduced a novel equivariant framework based on Spin-Weighted Spherical Harmonics (SWSH), bridging the gap between the computational efficiency of Gaunt-based tensor products and the mathematical completeness of the Clebsch-Gordan Tensor Product. By leveraging the spin-weight degree of freedom, we recover the antisymmetric paths essential for resolving chiral geometries. Theoretically, we demonstrate that the SWSH basis captures odd-parity interactions through specialized spin-selection rules. Architecturally, we proposed equivariant SWSH linear and normalization layers that enforce strict symmetry constraints while optimizing for hardware throughput. Empirically, our framework demonstrates superior expressivity across diverse benchmarks. These results suggest that SWSH-based equivariant networks offer a robust and scalable solution for high-fidelity geometric modeling in molecular science and beyond.

Acknowledgments

This work was supported in part by the National Science Foundation under Grants IIS-2243850, CNS-2328395, and MOMS-2331036; the National Institutes of Health under Grant U01AG070112; the Texas A&M University Division of Research Targeted Proposal Teams Funding Program; and the Texas A&M Institute of Data Science Thematic Labs Program.

References

- [1] Brandon Anderson, Truong Son Hy, and Risi Kondor. Cormorant: Covariant molecular neural networks. *Advances in neural information processing systems*, 32, 2019.
- [2] Ilyes Batatia, David P Kovacs, Gregor Simm, Christoph Ortner, and Gábor Csányi. Mace: Higher order equivariant message passing neural networks for fast and accurate force fields. *Advances in neural information processing systems*, 35:11423–11436, 2022.
- [3] Ilyes Batatia, Simon Batzner, Dávid Péter Kovács, Albert Musaelian, Gregor NC Simm, Ralf Drautz, Christoph Ortner, Boris Kozinsky, and Gábor Csányi. The design space of $e(3)$ -equivariant atom-centred interatomic potentials. *Nature Machine Intelligence*, 7(1):56, 2025.
- [4] Simon Batzner, Albert Musaelian, Lixin Sun, Mario Geiger, Jonathan P Mailoa, Mordechai Kornbluth, Nicola Molinari, Tess E Smidt, and Boris Kozinsky. $E(3)$ -equivariant graph neural networks for data-efficient and accurate interatomic potentials. *Nature communications*, 13(1):2453, 2022.
- [5] Michael M Bronstein, Joan Bruna, Taco Cohen, and Petar Veličković. Geometric deep learning: Grids, groups, graphs, geodesics, and gauges. *arXiv preprint arXiv:2104.13478*, 2021.
- [6] Lowik Chanussot, Abhishek Das, Siddharth Goyal, Thibaut Lavril, Muhammed Shuaibi, Morgane Riviere, Kevin Tran, Javier Heras-Domingo, Caleb Ho, Weihua Hu, et al. Open catalyst 2020 (oc20) dataset and community challenges. *Acs Catalysis*, 11(10):6059–6072, 2021.
- [7] Jiajun Fei and Zhidong Deng. Rotation invariance and equivariance in 3d deep learning: a survey. *Artificial Intelligence Review*, 57(7):168, 2024.
- [8] Cong Fu, Yuchao Lin, Zachary Krueger, Haiyang Yu, Maho Nakata, Jianwen Xie, Emine Kucukbenli, Xiaofeng Qian, and Shuiwang Ji. Augmenting molecular graphs with geometries via machine learning interatomic potentials. *arXiv preprint arXiv:2507.00407*, 2025.
- [9] Johannes Gasteiger, Shankari Giri, Johannes T Margraf, and Stephan Günnemann. Fast and uncertainty-aware directional message passing for non-equilibrium molecules. *arXiv preprint arXiv:2011.14115*, 2020.
- [10] Johannes Gasteiger, Florian Becker, and Stephan Günnemann. Gemnet: Universal directional graph neural networks for molecules. *Advances in neural information processing systems*, 34:6790–6802, 2021.
- [11] Mario Geiger, Tess Smidt, Alby M., Benjamin Kurt Miller, Wouter Boomsma, Bradley Dice, Kostiantyn Lapchevskyi, Maurice Weiler, Michał Tyszkiewicz, Simon Batzner, Dylan Madisetti, Martin Uhrin, Jes Frellsen, Nuri Jung, Sophia Sanborn, Mingjian Wen, Josh Rackers, Marcel Rød, and Michael Bailey. Euclidean neural networks: e3nn, April 2022. URL <https://doi.org/10.5281/zenodo.6459381>.

- [12] Joshua N Goldberg, Alan J MacFarlane, Ezra T Newman, Fritz Rohrllich, and EC George Sudarshan. Spin-s spherical harmonics and δ . *Journal of Mathematical Physics*, 8(11):2155–2161, 1967.
- [13] Mojtaba Haghighatlari, Jie Li, Xingyi Guan, Oufan Zhang, Akshaya Das, Christopher J Stein, Farnaz Heidar-Zadeh, Meili Liu, Martin Head-Gordon, Luke Bertels, et al. Newtonnet: a newtonian message passing network for deep learning of interatomic potentials and forces. *Digital Discovery*, 1(3):333–343, 2022.
- [14] Dennis M Healy Jr, Daniel N Rockmore, Peter J Kostelec, and Sean Moore. Ffts for the 2-sphere-improvements and variations. *Journal of Fourier analysis and applications*, 9(4):341–385, 2003.
- [15] Valery Kelmanovich Khersonskii, Anatoly Nikolaevich Moskalev, and Dmitry Alexandrovich Varshalovich. *Quantum theory of angular momentum*. World Scientific, 1988.
- [16] Risi Kondor. The principles behind equivariant neural networks for physics and chemistry. *Proceedings of the National Academy of Sciences*, 122(41):e2415656122, 2025.
- [17] Dávid Péter Kovács, J Harry Moore, Nicholas J Browning, Ilyes Batatia, Joshua T Horton, Yixuan Pu, Venkat Kapil, William C Witt, Ioan-Bogdan Magdau, Daniel J Cole, et al. Mace-off: Short-range transferable machine learning force fields for organic molecules. *Journal of the American Chemical Society*, 147(21):17598–17611, 2025.
- [18] Dávid Péter Kovács, Cas van der Oord, Jiri Kucera, Alice E. A. Allen, Daniel J. Cole, Christoph Ortner, and Gábor Csányi. Linear atomic cluster expansion force fields for organic molecules: Beyond rmse. *Journal of Chemical Theory and Computation*, 17(12):7696–7711, 2021. doi: 10.1021/acs.jctc.1c00647. URL <https://doi.org/10.1021/acs.jctc.1c00647>. PMID: 34735161.
- [19] Greg Landrum, Paolo Tosco, Brian Kelley, Ricardo Rodriguez, David Cosgrove, Riccardo Vianello, sriniker, Peter Gedeck, Gareth Jones, Eisuke Kawashima, NadineSchneider, Dan Nealschneider, tadhurst cdd, Andrew Dalke, Matt Swain, Brian Cole, Samo Turk, Aleksandr Savelev, Niels Maeder, Yakov Pechersky, Alain Vaucher, Maciej Wójcikowski, Rachel Walker, Hussein Faara, Ichiru Take, Vincent F. Scalfani, Daniel Probst, Kazuya Ujihara, Jeremy Monat, and Juuso Lehtivarjo. rdkit/rdkit: 2026_03_2 (q1 2026) release, April 2026. URL <https://doi.org/10.5281/zenodo.19922430>.
- [20] Yunyang Li, Lin Huang, Zhihao Ding, Xinran Wei, Chu Wang, Han Yang, Zun Wang, Chang Liu, Yu Shi, Peiran Jin, Tao Qin, Mark Gerstein, and Jia Zhang. E2former: An efficient and equivariant transformer with linear-scaling tensor products. In *The Thirty-ninth Annual Conference on Neural Information Processing Systems*, 2026. URL <https://openreview.net/forum?id=ls5L4IMEwt>.
- [21] Yi-Lun Liao and Tess Smidt. Equiformer: Equivariant graph attention transformer for 3d atomistic graphs. In *The Eleventh International Conference on Learning Representations*, 2023. URL <https://openreview.net/forum?id=KwmPfARgOTD>.
- [22] Yi-Lun Liao, Brandon M Wood, Abhishek Das, and Tess Smidt. Equiformerv2: Improved equivariant transformer for scaling to higher-degree representations. In *The Twelfth International Conference on Learning Representations*, 2024. URL <https://openreview.net/forum?id=mCOBKZmrzD>.
- [23] Yuchao Lin, Cong Fu, Zachary Krueger, Haiyang Yu, Maho Nakata, Jianwen Xie, Emine Kucukbenli, Xiaofeng Qian, and Shuiwang Ji. Tensor decomposition networks for accelerating machine learning force field computations. In *The Thirty-ninth Annual Conference on Neural Information Processing Systems*, 2025. URL <https://openreview.net/forum?id=9vKJyCUfMH>.

- [24] Yi Liu, Limei Wang, Meng Liu, Yuchao Lin, Xuan Zhang, Bora Oztekin, and Shuiwang Ji. Spherical message passing for 3D molecular graphs. In *International Conference on Learning Representations*, 2022.
- [25] Shengjie Luo, Tianlang Chen, and Aditi S Krishnapriyan. Enabling efficient equivariant operations in the fourier basis via gaunt tensor products. In *The Twelfth International Conference on Learning Representations*, 2024.
- [26] Albert Musaelian, Simon Batzner, Anders Johansson, Lixin Sun, Cameron J Owen, Mordechai Kornbluth, and Boris Kozinsky. Learning local equivariant representations for large-scale atomistic dynamics. *Nature Communications*, 14(1):579, 2023.
- [27] Saro Passaro and C Lawrence Zitnick. Reducing so (3) convolutions to so (2) for efficient equivariant gnns. In *International conference on machine learning*, pages 27420–27438. PMLR, 2023.
- [28] Christian Reisswig, Nigel Bishop, and Denis Pollney. General relativistic null-cone evolutions with a high-order scheme. *General Relativity and Gravitation*, 45(5):1069–1094, 2013.
- [29] Kristof Schütt, Pieter-Jan Kindermans, Huziel Enoc Saucedo Felix, Stefan Chmiela, Alexandre Tkatchenko, and Klaus-Robert Müller. Schnet: A continuous-filter convolutional neural network for modeling quantum interactions. *Advances in neural information processing systems*, 30, 2017.
- [30] Kristof Schütt, Oliver Unke, and Michael Gastegger. Equivariant message passing for the prediction of tensorial properties and molecular spectra. In *International conference on machine learning*, pages 9377–9388. PMLR, 2021.
- [31] Nathaniel Thomas, Tess Smidt, Steven Kearnes, Lusann Yang, Li Li, Kai Kohlhoff, and Patrick Riley. Tensor field networks: Rotation-and translation-equivariant neural networks for 3d point clouds. *arXiv preprint arXiv:1802.08219*, 2018.
- [32] Soledad Villar, David W Hogg, Kate Storey-Fisher, Weichi Yao, and Ben Blum-Smith. Scalars are universal: Equivariant machine learning, structured like classical physics. *Advances in neural information processing systems*, 34:28848–28863, 2021.
- [33] Limei Wang, Yi Liu, Yuchao Lin, Haoran Liu, and Shuiwang Ji. Comenet: Towards complete and efficient message passing for 3d molecular graphs. *Advances in Neural Information Processing Systems*, 35:650–664, 2022.
- [34] Yuqing Xie, Ameya Daigavane, Mit Kotak, and Tess Smidt. The price of freedom: Exploring expressivity and runtime tradeoffs in equivariant tensor products. In *International Conference on Machine Learning*, pages 68599–68625. PMLR, 2025.
- [35] YuQing Xie, Ameya Daigavane, Mit Kotak, and Tess Smidt. Asymptotically fast clebsch-gordan tensor products with vector spherical harmonics. *arXiv preprint arXiv:2602.21466*, 2026.
- [36] Xuan Zhang, Limei Wang, Jacob Helwig, Youzhi Luo, Cong Fu, Yaochen Xie, Meng Liu, Yuchao Lin, Zhao Xu, Keqiang Yan, et al. Artificial intelligence for science in quantum, atomistic, and continuum systems. *Foundations and Trends® in Machine Learning*, 18(4):385–849, 2025.

A. Spin-Weighted Spherical Harmonics (SWSH)

Spin-weighted spherical harmonics (SWSH), denoted as ${}_s Y_{\ell m}(\theta, \phi)$, are generalizations of the standard spherical harmonics $Y_{\ell m}$. Unlike ordinary spherical harmonics, which are scalar fields, spin-weighted harmonics are functions on the sphere that behave as U(1) gauge fields, characterized by a degree ℓ , a magnetic order m , and a spin weight s satisfying $|s| \leq \ell$.

In the standard case where $s = 0$, these functions reduce to the conventional scalar spherical harmonics, such that ${}_0 Y_{\ell m} = Y_{\ell m}$. Like their scalar counterparts, SWSHs form a complete orthonormal basis over the sphere S^2 , satisfying the orthogonality condition:

$$\int_{S^2} {}_s Y_{\ell m} {}_s Y_{\ell' m'}^* d\Omega = \delta_{\ell\ell'} \delta_{mm'}. \quad (11)$$

This orthonormality, combined with their unique transformation properties under local rotations, makes them ideal for representing high-dimensional equivariant features that standard scalar bases cannot fully capture.

A.1. Explicit Formula

The spin-weighted spherical harmonics can be calculated directly using the formula [12]

$$\begin{aligned} {}_s Y_{\ell m}(\theta, \phi) &= A_{s\ell m} \sin^{2\ell} \left(\frac{\theta}{2} \right) e^{im\phi} \\ &\times \sum_{r=0}^{\ell-s} (-1)^r \binom{\ell-s}{r} \binom{\ell+s}{r+s-m} \\ &\times \cot^{2r+s-m} \left(\frac{\theta}{2} \right). \end{aligned} \quad (12)$$

Specifically, the first few spin-weighted spherical harmonics for $s = 1$ and $\ell = 1$ are given by

$${}_1 Y_{10}(\theta, \phi) = \sqrt{\frac{3}{8\pi}} \sin \theta, \quad {}_1 Y_{1\pm 1}(\theta, \phi) = -\sqrt{\frac{3}{16\pi}} (1 \mp \cos \theta) e^{\pm i\phi}. \quad (13)$$

With the phase convention used in this definition, the harmonics satisfy the following conjugation and parity relations

$${}_s Y_{\ell m}^* = (-1)^{s+m} {}_{-s} Y_{\ell(-m)}, \quad {}_s Y_{\ell m}(\pi - \theta, \phi + \pi) = (-1)^\ell {}_{-s} Y_{\ell m}(\theta, \phi). \quad (14)$$

A.2. Equivariance and Spin-Weighted Transformations

A defining characteristic of spin-weighted spherical harmonics is their transformation law under the rotation group SO(3). Unlike standard scalar harmonics ($s = 0$), which transform solely via the Wigner D -matrices, SWSHs are sections of a line bundle and thus pick up a local phase shift corresponding to the rotation of the local tangent frame.

Rotation Law. Given a rotation $R \in \text{SO}(3)$, the transformation of a spin-weighted signal at a point $\mathbf{x} \in \mathbb{S}^2$ is governed by:

$${}_s Y_{\ell m}(R\mathbf{x}) = e^{is\psi(R,\mathbf{x})} \sum_{m'=-\ell}^{\ell} D_{m'm}^{(\ell)}(R) {}_s Y_{\ell m'}(\mathbf{x}) \quad (15)$$

where $D_{m'm}^{(\ell)}(R)$ are the elements of the $(2\ell + 1)$ -dimensional irreducible representation of $\text{SO}(3)$. The term $e^{is\psi}$ represents a $\text{U}(1)$ gauge transformation, where $\psi(R, \mathbf{x})$ is the angle by which the local tangent frame at \mathbf{x} rotates relative to the fixed coordinate basis after applying R .

Geometry-Dependent Frames. In our implementation, the gauge is fixed by equivariant frames constructed from the input geometry. Before evaluating SWSHs, the input is rotated into a common frame. We implement both the global frame and local node frame based on the geometry.

For the **global frame**, given a graph b and point cloud $\{\mathbf{x}_i\}_{i \in b}$, let

$$\mathbf{c}_b = \sum_{i \in b} w_i \mathbf{x}_i, \quad \tilde{\mathbf{x}}_i = \mathbf{x}_i - \mathbf{c}_b.$$

We construct a graph frame $F_b \in \text{SO}(3)$ from the eigensystem of the centered covariance

$$C_b = \sum_{i \in b} w_i \tilde{\mathbf{x}}_i \tilde{\mathbf{x}}_i^\top. \quad (16)$$

The eigenvector signs are fixed by parity-even axial references

$$\mathbf{h}_b^{(q)} = \sum_{i \in b} w_i \|\tilde{\mathbf{r}}_i\|^q \tilde{\mathbf{r}}_i, \quad \mathbf{a}_b = \mathbf{h}_b^{(1)} \times \mathbf{h}_b^{(2)}, \quad \mathbf{b}_b = \mathbf{h}_b^{(2)} \times \mathbf{h}_b^{(3)}.$$

If no repeated eigenvalues and vanishing axial references are present, this gives a permutation-equivariant, $\text{SO}(3)$ -equivariant, and parity-invariant graph frame.

If the global frame encounters eigenvector ambiguity, we use the **local node frame**. For each node j , we similarly construct a local node frame $F_j \in \text{SO}(3)$ from the neighborhood quadrupole

$$Q_j = \sum_{k \rightarrow j} w_{jk} \left(\|\mathbf{r}_{jk}\|^2 I - \mathbf{r}_{jk} \mathbf{r}_{jk}^\top \right), \quad (17)$$

where $\mathbf{r}_{jk} = \mathbf{x}_j - \mathbf{x}_k$. Given $\mathbf{g}_j = \sum_{k \rightarrow j} w_{jk} \mathbf{r}_{jk}$, the eigenvector signs are fixed by axial references

$$\mathbf{h}_j^{(q)} = \sum_{k \rightarrow j} w_{jk} \|\mathbf{r}_{jk}\|^q \mathbf{r}_{jk}, \quad \mathbf{a}_j = \mathbf{h}_j^{(1)} \times \mathbf{g}_j, \quad \mathbf{b}_j = \mathbf{h}_j^{(2)} \times \mathbf{g}_j.$$

This also gives a permutation-equivariant, $\text{SO}(3)$ -equivariant, and parity-invariant node frame whenever the local neighborhood is nondegenerate.

A.3. Nonzero Spin-Weighted Gaunt Paths

The spin-weighted Gaunt coefficient is

$$G_{(\ell_1, m_1, s_1)(\ell_2, m_2, s_2)}^{(\ell_3, m_3, s_3)} = \sqrt{\frac{\prod_{i=1}^3 (2\ell_i + 1)}{4\pi}} \begin{pmatrix} \ell_1 & \ell_2 & \ell_3 \\ m_1 & m_2 & -m_3 \end{pmatrix} \begin{pmatrix} \ell_1 & \ell_2 & \ell_3 \\ s_1 & s_2 & -s_3 \end{pmatrix}. \quad (18)$$

The scalar GTP case fixes $s_1 = s_2 = s_3 = 0$, so the second Wigner symbol vanishes whenever $\ell_1 + \ell_2 + \ell_3$ is odd. Allowing signed spin weights removes this limitation at the path level.

Proposition 2: Spin-weighted path completion

Let (ℓ_1, ℓ_2, ℓ_3) satisfy the Clebsch-Gordan triangle rule. Then there exist signed spin weights

$$s_1 \in [-\ell_1, \ell_1], \quad s_2 \in [-\ell_2, \ell_2], \quad s_3 \in [-\ell_3, \ell_3],$$

with $s_3 = s_1 + s_2$, such that the signed-spin path $(\ell_1, s_1) \otimes (\ell_2, s_2) \rightarrow (\ell_3, s_3)$ is not identically zero.

Proof. Choose

$$s_1 = \ell_1, \quad s_2 = \ell_3 - \ell_1, \quad s_3 = \ell_3.$$

Then $s_3 = s_1 + s_2$ and $-\ell_2 \leq \ell_3 - \ell_1 \leq \ell_2$, so all chosen spin weights are admissible. Consider the spin Wigner factor

$$S = \begin{pmatrix} \ell_1 & \ell_2 & \ell_3 \\ \ell_1 & \ell_3 - \ell_1 & -\ell_3 \end{pmatrix}.$$

For this boundary case, the Wigner $3j$ symbol has the explicit magnitude

$$|S| = \left[\frac{(2\ell_1)!(2\ell_3)!}{(\ell_1 - \ell_2 + \ell_3)!(\ell_1 + \ell_2 + \ell_3 + 1)!} \right]^{1/2}.$$

All factorial arguments are nonnegative by the triangle inequalities, so $S \neq 0$. For these fixed spin weights, the spin-weighted Gaunt coefficient factors as

$$G_{(\ell_1, m_1, s_1)(\ell_2, m_2, s_2)}^{(\ell_3, m_3, s_3)} = \sqrt{\frac{\prod_{i=1}^3 (2\ell_i + 1)}{4\pi}} \begin{pmatrix} \ell_1 & \ell_2 & \ell_3 \\ m_1 & m_2 & -m_3 \end{pmatrix} S.$$

Taking

$$m_1 = \ell_1, \quad m_2 = \ell_3 - \ell_1, \quad m_3 = \ell_3$$

gives the same nonzero Wigner factor in the magnetic part. Hence

$$G_{(\ell_1, m_1, s_1)(\ell_2, m_2, s_2)}^{(\ell_3, m_3, s_3)} = \sqrt{\frac{\prod_{i=1}^3 (2\ell_i + 1)}{4\pi}} S^2 \neq 0.$$

Therefore the signed-spin Gaunt tensor has a nonzero entry and the corresponding bilinear map is not identically zero. \square

B. Best Asymptotic Runtime Cost

Proposition 3: Runtime complexity for $|s|_{\max} = 1$

Given bounded multiplicities and a maximum angular degree L , a fully connected SpinGTP can be evaluated in $O(L^4 \log^2 L)$ using fast spherical transforms.

Proof. Let degrees $0 \leq \ell_1, \ell_2 \leq L$ and spin weights $-1 \leq s_1, s_2 \leq 1$. Define the spherical signals

$$f(\Omega) = \sum_{m_1=-\ell_1}^{\ell_1} x_{\ell_1 m_1 s_1}^{(1)} Y_{\ell_1 m_1}(\Omega) \quad \text{and} \quad g(\Omega) = \sum_{m_2=-\ell_2}^{\ell_2} x_{\ell_2 m_2 s_2}^{(2)} Y_{\ell_2 m_2}(\Omega). \quad (19)$$

For $s_3 = s_1 + s_2$, the coefficient of the pointwise product of $f(\Omega)$ and $g(\Omega)$ is

$$\int_{\mathbb{S}^2} f(\Omega) g(\Omega) s_3 Y_{\ell_3 m_3}^*(\Omega) d\Omega = \sum_{m_1, m_2} G_{(\ell_1, m_1, s_1)(\ell_2, m_2, s_2)}^{(\ell_3, m_3, s_3)} x_{\ell_1 m_1 s_1}^{(1)} x_{\ell_2 m_2 s_2}^{(2)}. \quad (20)$$

Thus, a tensor product path of $(\ell_1, s_1, \ell_2, s_2)$ is evaluated by two inverse spherical transforms, one pointwise product, and one forward spherical transform. Since $\ell_3 \leq \ell_1 + \ell_2 \leq 2L$, the forward and backward transform costs $O(L^2 \log^2 L)$ using fast spherical transform algorithm [14]. The pointwise multiplication itself costs $O(L^2)$. Therefore, a path of $(\ell_1, s_1, \ell_2, s_2)$ costs $O(L^2 \log^2 L) + O(L^2) = O(L^2 \log^2 L)$.

There are $(L+1)^2 = O(L^2)$ input degree pairs of (ℓ_1, ℓ_2) . These pairs are evaluated separately for the independent path weights in Equation (7). Each spherical transform returns all admissible output degrees ℓ_3 simultaneously, so no additional factor of L is required. Consequently, the time complexity of SpinGTP is

$$\begin{aligned} T_{\text{SpinGTP}}(L) &= O(L^2) \times O(L^2 \log^2 L) \\ &= O(L^4 \log^2 L). \end{aligned} \quad (21)$$

This is the same asymptotic cost as the complete VSTP of [35]. \square

C. Real Basis Spin-Weighted Spherical Harmonics

In computational physics and deep learning, while complex-valued representations are mathematically natural, real-valued features are often preferred for memory efficiency and compatibility with standard nonlinearities. We therefore store SWSH features in a real orthonormal basis and use a unitary change of basis only when evaluating complex Gaunt contractions.

C.1. The Unitary \mathbf{Q} Matrix

Let \mathbf{a}_{real} denote real-basis coefficients and $\mathbf{a}_{\text{complex}}$ denote complex SWSH coefficients. We use a unitary matrix \mathbf{Q} such that

$$\mathbf{a}_{\text{complex}} = \mathbf{Q} \mathbf{a}_{\text{real}}, \quad \mathbf{a}_{\text{real}} = \text{Re}(\mathbf{Q}^\dagger \mathbf{a}_{\text{complex}}). \quad (22)$$

For the scalar case $|s| = 0$, $\mathbf{Q} \in \mathbb{C}^{(2\ell+1) \times (2\ell+1)}$. With rows and columns indexed by $m, k \in \{-\ell, \dots, \ell\}$, the matrix elements used in our implementation are

$$\mathbf{Q}_{m,k} = \begin{cases} 1 & \text{if } m = 0, k = 0, \\ \frac{1}{\sqrt{2}} & \text{if } m > 0, k = m, \\ \frac{i}{\sqrt{2}} & \text{if } m > 0, k = -m, \\ \frac{(-1)^{|m|}}{\sqrt{2}} & \text{if } m < 0, k = |m|, \\ \frac{-i(-1)^{|m|}}{\sqrt{2}} & \text{if } m < 0, k = -|m|, \\ 0 & \text{otherwise.} \end{cases} \quad (23)$$

For $|s| > 0$, both signed spin sectors s and $-s$ are retained. The corresponding matrix has size

$$\mathbf{Q} \in \mathbb{C}^{2(2\ell+1) \times 2(2\ell+1)},$$

with the complex coefficients ordered by the $-|s|$ sector followed by the $|s|$ sector. This doubled matrix couples the paired $\pm s$ and $\pm m$ components using Equation (5).

C.2. Example: The Q Matrix for $\ell = 1$

For $\ell = 1$ and $|s| = 0$, with both rows and columns ordered as $(-1, 0, +1)$, the transformation matrix is

$$\mathbf{Q}^{(1)} = \frac{1}{\sqrt{2}} \begin{pmatrix} i & 0 & -1 \\ 0 & \sqrt{2} & 0 \\ i & 0 & 1 \end{pmatrix}. \quad (24)$$

By using this, real coefficients are mapped to the complex signed-spin basis, the generalized Gaunt contraction is evaluated, and the result is mapped back to the real basis using \mathbf{Q}^\dagger .

D. Derivation of the Parity-Equivariant Basis

A signal $f(\mathbf{x})$ is said to possess a definite parity $p \in \{+1, -1\}$ if, under the spatial inversion operator $P : \mathbf{x} \rightarrow -\mathbf{x}$, it satisfies the equivariance relation:

$$f(P\mathbf{x}) = pf(\mathbf{x}). \quad (25)$$

For standard scalar spherical harmonics ($s = 0$), parity is intrinsically tied to the degree ℓ , where $Y_{\ell m}(-\mathbf{x}) = (-1)^\ell Y_{\ell m}(\mathbf{x})$. However, spin-weighted spherical harmonics exhibit a more complex behavior under inversion. As shown in Appendix A.1, the parity transformation for SWSH involves a simultaneous inversion of the spin weight:

$${}_s Y_{\ell m}(-\mathbf{x}) = (-1)^\ell {}_{-s} Y_{\ell m}(\mathbf{x}). \quad (26)$$

Because the inversion maps a function of spin weight s to a function of spin weight $-s$, the individual basis functions do not possess a well-defined parity unless $s = 0$. This same coupling persists in the real-basis representation ${}_s R_{\ell m}$ defined in Eq. 5:

$${}_s R_{\ell m}(-\mathbf{x}) = (-1)^\ell {}_{-s} R_{\ell m}(\mathbf{x}). \quad (27)$$

To construct a basis that satisfies the parity-equivariance constraint in Eq. 25, we seek a linear combination of the spin-doubled basis functions. We define the Parity-Equivariant SWSH Basis, denoted $\mathcal{R}_p^{s,\ell,m}(\mathbf{x})$, as:

$$\mathcal{R}_p^{s,\ell,m}(\mathbf{x}) = \frac{1}{\sqrt{2}} \left({}_{-s} R_{\ell m}(\mathbf{x}) + p(-1)^\ell {}_s R_{\ell m}(\mathbf{x}) \right). \quad (28)$$

Proposition 4: Parity Equivariance

$\mathcal{R}_p^{s,\ell,m}$ satisfies parity equivariance relation Equation (25).

Proof. To verify that this construction yields a basis with parity p , we apply the inversion operator P such that

$$\begin{aligned}
 \mathcal{R}_p^{s,\ell,m}(-\mathbf{x}) &= \frac{1}{\sqrt{2}} \left(-{}_sR_{\ell m}(-\mathbf{x}) + p(-1)^\ell {}_sR_{\ell m}(-\mathbf{x}) \right) \\
 &= \frac{1}{\sqrt{2}} \left((-1)^\ell {}_sR_{\ell m}(\mathbf{x}) + p(-1)^\ell (-1)^\ell -{}_sR_{\ell m}(\mathbf{x}) \right) \\
 &= \frac{1}{\sqrt{2}} \left((-1)^\ell {}_sR_{\ell m}(\mathbf{x}) + p -{}_sR_{\ell m}(\mathbf{x}) \right) \\
 &= p \left(\frac{1}{\sqrt{2}} \left(-{}_sR_{\ell m}(\mathbf{x}) + \frac{(-1)^\ell}{p} {}_sR_{\ell m}(\mathbf{x}) \right) \right) \\
 &= p \left(\frac{1}{\sqrt{2}} \left(-{}_sR_{\ell m}(\mathbf{x}) + p(-1)^\ell {}_sR_{\ell m}(\mathbf{x}) \right) \right) \\
 &= p\mathcal{R}_p^{s,\ell,m}(\mathbf{x}).
 \end{aligned} \tag{29}$$

□

This derivation confirms that the basis $\mathcal{R}_p^{s,\ell,m}(\mathbf{x})$ adheres strictly to the prescribed parity p . By decoupling the parity-even ($p = +1$) and parity-odd ($p = -1$) sectors, this formulation allows the network to explicitly represent pseudoscalar and axial-vector interactions, which are essential for resolving the antisymmetry gap in chiral geometric modeling.

E. SpinGTP Implementation and Time Comparison

We follow a similar implementation style with respect to e3nn [11].

E.1. Tensor Product Implementation

Multiplicity connection modes. All SpinGTP variants use the same real SWSH Gaunt kernel. For one instruction involving irreps $\rho_1 = (\ell_1, |s_1|, p_1)$, $\rho_2 = (\ell_2, |s_2|, p_2)$, and $\rho_3 = (\ell_3, |s_3|, p_3)$ with $p_3 = p_1 p_2$, let

$$\mathbf{K}_{\rho_1, \rho_2}^{\rho_3}(m_1, m_2, m_3) \tag{30}$$

denote the real-basis SpinGTP kernel obtained from the signed-spin Gaunt contraction G and parity recombination described in Equation (7). Here m_1, m_2, m_3 index the real irrep components, and u, v, w index multiplicity channels. The different tensor-product layers differ only in how the multiplicity indices are connected.

Fully connected tensor product. The fully connected mode (mode uvw) enumerates all admissible irrep-block pairs (ρ_1, ρ_2) and all requested output irreps $\rho_3 \in \rho_1 \otimes \rho_2$. For each instruction, it first forms

$$R_{uv, m_3} = \sum_{m_1, m_2} \mathbf{K}_{\rho_1, \rho_2}^{\rho_3}(m_1, m_2, m_3) \mathbf{x}_{u, m_1}^{(1)} \mathbf{x}_{v, m_2}^{(2)}, \tag{31}$$

and then applies a learned dense multiplicity mixing

$$[\mathbf{x}^{(1)} \otimes_{\mathbf{W}} \mathbf{x}^{(2)}]^{(w, m_3)} = \sum_{u=1}^U \sum_{v=1}^V \mathbf{W}_{uvw} R_{uv, m_3}. \tag{32}$$

The parameter count per instruction is UVW .

Depthwise tensor product. The depthwise mode (mode uvu) is fully connected over admissible irrep-block pairs, but preserves the first input multiplicity channel. For each instruction, the output multiplicity is tied to the first input multiplicity ($w = u$), and the layer computes

$$[\mathbf{x}^{(1)} \otimes_{\mathbf{W}} \mathbf{x}^{(2)}]^{(u,m_3)} = \sum_{v=1}^V \mathbf{W}_{uv} \sum_{m_1, m_2} \mathbf{K}_{\rho_1, \rho_2}^{\rho_3}(m_1, m_2, m_3) \mathbf{x}_{u, m_1}^{(1)} \mathbf{x}_{v, m_2}^{(2)}. \quad (33)$$

In the molecular message-passing setting, the second input is usually an edge basis with $V = 1$. Following Equation (8) and (9) in the main text, we utilize the pre-contracted kernel \mathbf{K}_{pre} to evaluate the channel-depthwise form

$$[\mathbf{x}^{(1)} \otimes_{\mathbf{W}} \mathbf{x}^{(2)}]^{(u,m_3)} = \mathbf{W}_u \sum_{m_1} \mathbf{K}_{\text{pre}}^{\rho_3}(m_1, m_3) \mathbf{x}_{u, m_1}^{(1)}. \quad (34)$$

Thus the parameter count per instruction is UV , or U when $V = 1$. The optimized `cached_uv` and `triton_uv` backends are specialized for this common $V = 1$ edge-feature case.

Elementwise tensor product. The elementwise mode (mode uuu) pairs corresponding input irrep blocks and requires matching multiplicities. For each paired block, it computes channelwise products

$$R_{u, m_3} = \sum_{m_1, m_2} \mathbf{K}_{\rho_1, \rho_2}^{\rho_3}(m_1, m_2, m_3) \mathbf{x}_{u, m_1}^{(1)} \mathbf{x}_{u, m_2}^{(2)}, \quad (35)$$

followed by an optional per-channel weight

$$[\mathbf{x}^{(1)} \otimes_{\mathbf{W}} \mathbf{x}^{(2)}]^{(u,m_3)} = \mathbf{W}_u R_{u, m_3}. \quad (36)$$

It does not mix different multiplicity channels and only connects corresponding input block pairs. The parameter count per instruction is U .

E.2. Runtime Comparison

We benchmark SpinGTP at two levels, including the depthwise tensor-product kernel and the full Equiformer-style model. All timings use a single NVIDIA H200 GPU and report time after warmup.

Depthwise tensor-product backend. We compare three implementations of the same depthwise tensor product, including direct Gaunt contraction, precontracted execution, and Triton-fused precontracted execution. The benchmark uses edge multiplicity one, $s_{\text{max}} = 1$, and a depthwise path-expanded layout. The batch dimension is the number of independent edge-level tensor-product samples. We evaluate batch sizes $\{1, 32, 128, 1024\}$, and selectively report over these batch sizes for each multiplicity. For $L_{\text{max}} = 1, 2$, both input irreps and output irreps are up to L_{max} . For $L_{\text{max}} = 3$, the first input is capped at $L_{\text{max}}^{(1)} = 1$, while the second input and output remain at $L_{\text{max}} = 3$.

Precontraction gives a consistent order-of-magnitude improvement over direct Gaunt contraction. Triton-fused precontraction is fastest for most small- and medium-batch settings. At large B and high multiplicity, the standard precontracted implementation can be faster because its batched matrix multiplications better saturate tensor cores.

Table 6: Depthwise SpinGTP tensor-product runtime on H200. Times are median milliseconds over 20 iterations. B is the number of independent edge-level tensor-product samples per call. Speedups are relative to direct Gaunt contraction.

$L_{\max}^{(1)}$	$L_{\max}^{(2)}$	$L_{\max}^{(\text{out})}$	Multiplicity	B	Direct Gaunt (ms)	Precontracted (ms)	Triton Precontracted (ms)	Gaunt / Triton
1	1	1	16	128	5.460	0.537	0.120	45.4×
1	1	1	64	128	5.493	0.466	0.119	46.2×
1	1	1	128	128	4.562	0.443	0.115	39.7×
2	2	2	16	32	21.570	0.997	0.259	83.15×
2	2	2	64	32	29.912	1.769	0.748	39.99×
2	2	2	128	32	33.528	1.837	0.559	59.96×
2	2	2	16	128	16.144	0.999	0.258	62.5×
2	2	2	64	128	29.561	1.771	0.752	39.3×
2	2	2	128	128	33.306	1.838	0.572	58.2×
1	3	3	16	128	12.714	0.678	0.228	55.9×
1	3	3	64	128	20.610	1.080	0.608	33.9×
1	3	3	128	128	22.546	1.344	0.681	33.1×
2	2	2	64	1024	29.912	1.777	2.090	14.3×
1	3	3	64	1024	23.941	1.394	1.865	12.8×
1	3	3	128	1024	22.628	1.350	2.240	10.1×

End-to-end Equiformer timing at $s = 0$. We also compare the standard Equiformer against an Equiformer model using the SpinGTP tensor-product implementation. All SWSH irreps are constrained to $s = 0$, so the comparison isolates implementation speed. Both models use the same 6-layer Equiformer-style architecture, 5.0 Å cutoff, 500 maximum neighbors, 80 atoms per graph, no PBC, and energy-only forward evaluation.

The GTP-based model is $1.21\times$ - $1.89\times$ faster in forward evaluation. At practical batch sizes of 32-64 graphs, it sustains 65-72k atoms/s, compared with 38-44k atoms/s for the standard Equiformer. Because $s = 0$ is enforced, this gain comes from the tensor-product implementation.

Table 7: Full-model forward runtime for Equiformer and Equiformer with GTP at $s = 0$. Times are median milliseconds over 10 iterations.

Graphs	Atoms	Equiformer (ms)	GTP, $s = 0$ (ms)	Speedup	Equiformer (atoms/s)	GTP, $s = 0$ (atoms/s)
1	80	23.438	19.358	1.21×	3,413	4,133
4	320	27.144	19.283	1.41×	11,789	16,595
16	1,280	41.729	22.049	1.89×	30,674	58,053
32	2,560	67.695	39.385	1.72×	37,817	64,999
64	5,120	116.298	70.917	1.64×	44,025	72,197

F. Training Details

F.1. 3BPA

Architecture. For 3BPA, our model is built on top of MACE [2] with the following modifications. First, we use SWSH with $s_{max} = 1$ instead of regular spherical harmonics, so each directed edge carries both standard and spin-weighted geometric features up to $L_{max} = 3$. Second, the equivariant tensor product in each interaction block is replaced by the fully-connected SWSH tensor product, recovering the antisymmetric coupling paths absent from scalar GTP. Third, all linear layers throughout the network including embedding projections, skip connections, and readout layers, are replaced with the specialized SWSH linear layers described in section 3.6. Additionally, the $s = 0$ product basis uses the same body-ordered symmetric contraction as the MACE baseline, while $|s| > 0$ channels bypass the contraction and are updated via a linear map. Crucially, we add a graph frame as described in Appendix A.2 that assigns all edges within a molecule a shared gauge, making the scatter-sum over spin-weighted messages equivariant.

Training Procedure. We optimize a weighted energy-and-force loss using Adam (AMSGrad) at learning rate 1×10^{-2} and weight decay 5×10^{-7} , under a ReduceLROnPlateau schedule (factor 0.8, patience 50). An exponential moving average of model weights with decay 0.99 is maintained throughout training. We follow a two-stage scheme: in Stage 1, the model is trained for up to 2000 epochs with energy and force loss weights of 1 and 1000 respectively. In Stage 2, we fine-tune with an increased energy loss weight of 25 to better resolve energy differences between conformers, running for up to 250 epochs. Final results are reported from Stage 2 checkpoints selected on validation loss. All experiments use float32 precision with RMS-forces output scaling. All 3BPA experiments were run on a single NVIDIA RTX A6000 (48 GB) GPU, with each run taking approximately 63 GPU-hours (56 hours for Stage 1 and 7 hours for Stage 2). Full hyperparameters are summarized in Table 8.

F.2. SPICE-MACE-OFF Chiral Subset

F.2.1. Chirality Classification and Parity Generalization

Architecture. For chirality tasks, we adapt the SpinGTP framework to a graph classification objective by replacing the atomic energy readout with a global MLP-based head. The backbone utilizes spin-weighted spherical harmonics (SWSH) with $L_{max} = 2$ and $s_{max} = 2$ to encode the geometric sensitivity required for enantiomer differentiation. The hidden representation is defined by a specific irrep set: $64 \times (0,0)e + 64 \times (1,0)o + 8 \times (1,1)o + 64 \times (2,0)e$. To ensure a rigorous benchmark, baseline architectures including NequIP [4], MACE [2], and MACE-Gaunt [25] are integrated into the same pipeline using identical cutoff radii ($r_{max} = 5.0 \text{ \AA}$) and radial basis functions (Table 9).

Training Procedure. We evaluate model performance through two distinct protocols. First, Standard Classification involves a 2-class task (R vs. S) on a random 85/15 split, optimized via AdamW with a learning rate of 1×10^{-3} . Second, Parity Generalization evaluates the model’s ability to learn the underlying symmetry operation by training exclusively on R-chiral structures with a regression target of $y = +1$. Generalization is measured by sign accuracy on unseen S-chiral mirror images ($y = -1$). These experiments use Adam with a StepLR schedule and early stopping based on `acc_S` to capture the model’s peak generalization capability. We train models on 144 GB NVIDIA463 H200 GPUs. Detailed hyperparameter settings for both tasks are provided in Tables 9 and 10.

Table 8: Training Configuration for 3BPA.

Item	Setting
Random seeds	3, 8, 9
Cutoff Radius	5.0 Å
Radial basis	8 Bessel, 5 polynomial cutoff basis
Angular degree	$L_{\max} = 3, s_{\max} = 1$
Interactions	2
Correlation order	3
Hidden irreps	$256 \times (0,0)e + 256 \times (1,0)o + 256 \times (2,0)e + 16 \times (1,1)o$
Readout MLP irreps	$16 \times (0,0)e$
Optimizer	Adam (AMSGrad)
Learning rate	1×10^{-2}
Weight decay	5×10^{-7}
LR schedule	ReduceLRonPlateau (factor 0.8, patience 50)
Batch size	5
EMA decay	0.99
Output scaling	RMS-forces scaling
Precision	float32
	<i>Stage 1</i> <i>Stage 2</i>
Energy loss weight	1 25
Force loss weight	1000 1000
Max epochs	2000 250
Patience	256 -

Table 9: Training Configuration for Chirality Classification.

Item	Setting
Task	2-class graph classification (R_only vs. S_only)
Data split	Random 85/15 train/validation split
Backbones	MACE, MACE-Gaunt, NequIP, SpinGTP
Cutoff	$r_{\max} = 5.0 \text{ Å}$
SWSH structure	$L_{\max} = 2, 2 \text{ interactions}, 8 \text{ Bessel}, 5 \text{ cutoff basis}$
SWSH hidden irreps	$64 \times (0,0)e + 64 \times (1,0)o + 8 \times (1,1)o + 64 \times (2,0)e$
Classifier head	MLP, hidden size 64, 2 output logits
Optimizer	AdamW
Learning rate	1×10^{-3}
Weight decay	1×10^{-5}
Batch size	16
Max epochs	200
LR schedule	ReduceLRonPlateau (factor 0.5, patience 10)

Table 10: Training Configuration for Parity Generalization.

Item	Setting
Task	Regression to parity target: $y = +1$ (R), $y = -1$ (S)
Train/test protocol	Train on R-only, evaluate on R-only and unseen S-only
Primary metric	Sign accuracy on unseen S (acc_S)
Loss	Mean-squared error (MSE)
Batch size	16
Max epochs	200
Learning rate	1×10^{-3}
Weight decay	1×10^{-5}
Patience	30 on acc_S
SWSH setup	$r_{\max} = 5.0$, mul=16, layers=2, $L_{\max} = 2$, $s_{\max} = 2$
Optimizer	Adam + StepLR (step=50, $\gamma = 0.5$)

F.2.2. Energy and Force Prediction

Architecture. We use the same SpinGTP architecture as our 3BPA experiments (Appendix F.1, Table 8): spin-weighted edge spherical harmonics with $s \in \{0, 1\}$, fully-connected SWSH tensor products in place of scalar Clebsch–Gordan contractions, SWSH linear layers throughout, body-ordered symmetric contraction for the $s = 0$ product basis with direct linear updates for $|s| > 0$ channels, and a shared graph frame that fixes a consistent gauge for spin-weighted messages (Appendix A.2). The only substantive differences for SPICE are the hidden/readout widths (Table 11) and the training-time tensor-product backend configuration used for throughput on large-scale dataset training.

Training Procedure. We optimize a weighted energy-and-force loss with weights 40 (energy) and 1000 (forces), using Adam (AMSGrad) at learning rate 1×10^{-2} and weight decay 5×10^{-10} , under a ReduceLROnPlateau schedule (factor 0.8, patience 50). An exponential moving average of the model weights with decay 0.99 is maintained throughout training. Training runs for up to 100 epochs with patience 50, using float32 precision and RMS-forces output scaling. We parallelize across 8 GPUs via PyTorch DDP with per-GPU batch size 32 (global batch 256). We train models on eight 144 GB NVIDIA463 H200 GPUs. Final results are reported from the best validation-loss checkpoint. All hyperparameters are summarized in Table 11.

F.3. OC20 IS2RE

Architecture. For OC20, we use an SWSH-Equiformer model built on the Equiformer attention backbone. The model uses on-the-fly periodic graphs with cutoff radius 5.0 \AA , at most 500 neighbors, and 128 radial basis functions. The standard equivariant tensor products, linear layers, and normalization layers are replaced by their SWSH counterparts. The main OC20 configuration keeps the persistent node and edge feature space bounded at $L_{\max} = 1$. Spin is introduced through a local spin head constructing bounded $|s| = 1$ SWSH templates $(1, 1)_o$ in the local node frame and applying a SpinGTP path

$$(1, 1)_o \otimes (1, 1)_o \rightarrow (1, 0)_e.$$

This head is enabled only in the attention activation path.

Table 11: Training configuration for Energy and Force Prediction on SPICE chiral subset.

Item	Setting
Random seed	9
Cutoff radius	5.0 Å
Radial basis	8 Bessel, 5 polynomial cutoff basis
Angular degree	$L_{\max} = 3, s_{\max} = 1$
Interactions	2
Correlation (body order)	3
Hidden irreps	$192 \times (0,0)_e + 192 \times (1,0)_o + 192 \times (2,0)_e + 12 \times (1,1)_o$
Readout MLP irreps	$12 \times (0,0)_e$
Product basis ($s = 0$)	body-ordered symmetric contraction (MACE)
Optimizer	Adam (AMSGrad)
Learning rate	1×10^{-2}
Weight decay	5×10^{-10}
LR schedule	ReduceLROnPlateau (factor 0.8, patience 50)
Energy loss weight	40
Force loss weight	1000
EMA decay	0.99
Output scaling	RMS-forces scaling
Batch size	32 per GPU (global 256, 8-GPU DDP)
Max epochs	190
Patience	50
Precision	float32

Training procedure. We train on OC20 IS2RE-DIRECT on a single NVIDIA H200 GPU without force regression or noisy-node auxiliary supervision. The model is optimized with AdamW and a cosine learning-rate schedule with warmup. Checkpoints are selected by validation energy error. The full configuration is summarized in Table 12.

Table 12: Training configuration for OC20 IS2RE-DIRECT.

Item	Setting
Task	OC20 IS2RE-DIRECT relaxed-energy prediction
Number of layers	6
Attention heads	8
Cutoff radius	5.0 Å
Max neighbors	500
Radial basis	128 Gaussian radial basis functions
Radial MLP	[64, 64]
Node embedding irreps	256x(0,0)e+128x(1,0)e
Edge SWSH irreps	1x(0,0)e+1x(1,0)e and 1x(1,1)o
Attention head irreps	32x(0,0)e+16x(1,0)e
MLP hidden irreps	768x(0,0)e+384x(1,0)e
Output feature irreps	512x(0,0)e
Optimizer	AdamW
Initial learning rate	2×10^{-4}
Weight decay	1×10^{-3}
Learning-rate schedule	Cosine LambdaLR
Warmup	2 epochs, warmup factor 0.2
Minimum LR factor	10^{-2}
Batch size	32
Evaluation batch size	32
Number of workers	16
EMA decay	0.999
Max epochs	20